

# Modelling and fabrication of GaAs photonic-crystal cavities for cavity quantum electrodynamics

U K Khankhoje<sup>1</sup>, S-H Kim<sup>1</sup>, B C Richards<sup>2</sup>, J Hendrickson<sup>2</sup>,  
J Sweet<sup>2</sup>, J D Olitzky<sup>2</sup>, G Khitrova<sup>2</sup>, H M Gibbs<sup>2</sup> and A Scherer<sup>1</sup>

<sup>1</sup> Electrical Engineering, California Institute of Technology, Pasadena, CA 91125, USA

<sup>2</sup> College of Optical Sciences, University of Arizona, Tucson, AZ 85721, USA

E-mail: [uday@caltech.edu](mailto:uday@caltech.edu)

Received 5 November 2009, in final form 14 December 2009

Published 8 January 2010

Online at [stacks.iop.org/Nano/21/065202](http://stacks.iop.org/Nano/21/065202)

## Abstract

In this paper, we present recent progress in the growth, modelling, fabrication and characterization of gallium arsenide (GaAs) two-dimensional (2D) photonic-crystal slab cavities with embedded indium arsenide (InAs) quantum dots (QDs) that are designed for cavity quantum electrodynamics (cQED) experiments. Photonic-crystal modelling and device fabrication are discussed, followed by a detailed discussion of different failure modes that lead to photon loss. It is found that, along with errors introduced during fabrication, other significant factors such as the presence of a bottom substrate and cavity axis orientation with respect to the crystal axis, can influence the cavity quality factor ( $Q$ ). A useful diagnostic tool in the form of contour finite-difference time domain (FDTD) is employed to analyse device performance.

(Some figures in this article are in colour only in the electronic version)

## 1. Introduction

Photonic-crystal cavities have come a long way from the initial conceptualization of photonic crystals [1, 2]. Sustained efforts in semiconductor growth, lithography and etching techniques have paved the way for the creation of high  $Q$ , low mode volume ( $V$ ) optical resonators that are ideally suited for exploring effects in quantum optics such as Purcell enhancement [3], vacuum Rabi splitting or strong coupling [4], and photon anti-bunching [5].

In our experiments, optical resonators are constructed by perturbing a 2D photonic crystal composed of a triangular lattice of air holes in a thin slab of GaAs (see figure 1(a)), and embedded InAs QDs serve as internal light sources. Typical resonator designs involve the creation of a defect by omission of one or more holes and/or the modification of the immediate neighbourhood of the missing air hole(s). Figure 1(b) demonstrates one such tuning process to get high  $Q/V$  resonant modes, in which two air holes are shifted by  $s$  [6]. In such a geometry, horizontal in-plane optical confinement is provided by the photonic bandgap [1] which can be nearly perfect as long as the cavity is surrounded by sufficiently many layers of photonic crystals. Incomplete

vertical confinement [7] happens on account of index contrast between the slab and the surrounding vacuum and is the primary cause of photon loss. The slab thickness is chosen such that only the lowest-order optical mode in the vertical direction is supported, thereby keeping the mode volume at a minimum and suppressing the coupling to the higher-order slab modes. Therefore, the slab thickness tends to be approximately close to half the wavelength of light in the material for optimal confinement.

This paper is dedicated to the modelling and fabrication of these devices, followed by a detailed investigation of the important channels for optical loss in these devices. Using three-dimensional (3D) FDTD methods and contour information extracted from the scanning electron micrograph (SEM) of a fabricated device, it is shown how various optical properties can be accurately analysed. Then, two important distinctive mechanisms of  $Q$  degradation will be emphasized; the presence of a bottom substrate and crystal-axis-dependent surface roughness resulting from the epitaxial growth process. As shown in the schematic in figure 1(a), a typical epi-structure for GaAs photonic-crystal slabs includes an optically flat bottom substrate. The sacrificial layer thickness is of the order

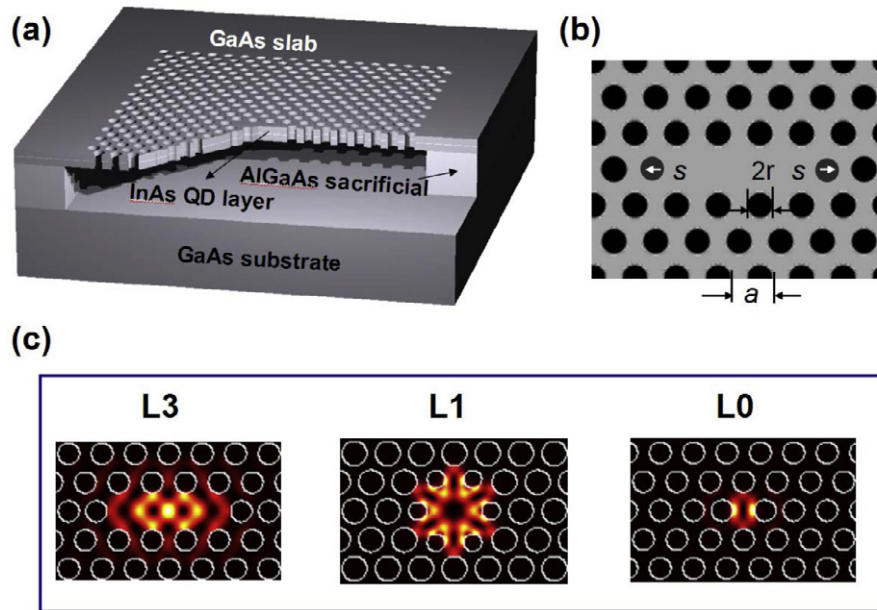


**Figure 1.** (a) Cutaway of a photonic-crystal-slab cavity. (b) Top view of the L3 cavity design.  $a$ ,  $r$ ,  $s$  are the lattice constant, radius and hole shifts, respectively. (c) In-plane (centre of slab) electric-field energy densities for three typical cavity designs; L3 (three missing holes, shifted end holes), L1 (one missing hole, shifted and shrunk nearest-neighbour holes) and L0 (no missing holes, only two shifted holes).

of  $\sim 1 \mu\text{m}$ , which has been chosen to be sufficiently larger than the evanescent tail of photonic-crystal cavity modes. However, it is still comparable to the free space emission wavelengths of InAs QDs used in this work. As a result, interesting interference effects originate from air-gap size-dependent resonances. The fabrication of these devices is fairly involved and challenging, and in our experiments we have come across several failure modes. Here, an attempt is made to catalogue these, and to suggest solutions where possible.

## 2. Photonic-crystal cavity modelling

For all the elegance of photonic crystals, a completely analytical description is illusive and hence these devices must be analysed numerically. Frequency-domain simulations [8] of the defect-free photonic-crystal slab reveal the extent of the photonic bandgap as a function of the in-plane Bloch wavevectors, as seen in figure 2. A subtlety must be mentioned at this point: since the structure only has 2D periodicity, light is (incompletely) confined in the vertical direction by total internal reflection. Therefore, any mode designated by  $(\omega, k)$  lying above the light line,  $\omega = ck$  ( $\omega$ ,  $c$ ,  $k$ : optical frequency, speed of light and in-plane wavevector, respectively) will always couple to the continuum of vacuum electromagnetic (radiation) modes. Thus, the photonic bandgap in this case is defined as the frequency range that is devoid of any guided modes [9] below the light line (i.e. for  $\omega < ck$ ) (radiation modes will exist at all frequencies). It should be noted that all guided bands can be divided into two groups depending on the mirror symmetry with respect to the plane in the middle of the slab; even and odd (or, equivalently, transverse electric (TE)-like or transverse magnetic (TM)-like, to invoke the similarities to their 2D counterparts). In the case of the triangular lattice

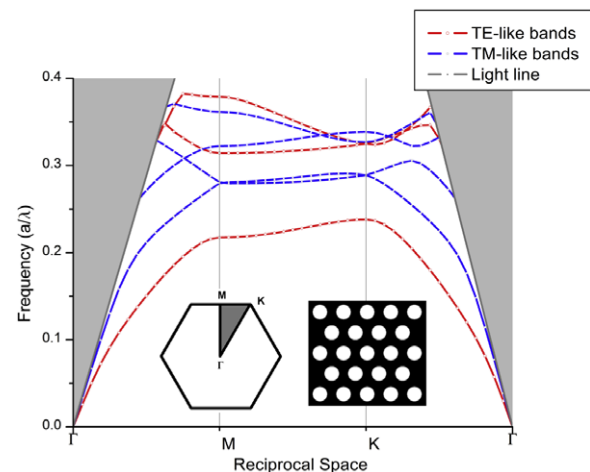


**Figure 2.** Dispersion diagram for TE-like (even) and TM-like (odd) modes of a 2D photonic-crystal slab composed of a triangular lattice of air holes (slab width,  $d$ , dielectric constant  $\epsilon$ ).  $r/a = 0.30$ ,  $d/a = 0.75$ ,  $\epsilon = 12.605$ . Insets show the reciprocal lattice space along with the irreducible Brillouin zone (shaded grey) and a real-space representation of a regular photonic crystal.

of air holes it is well known that a bandgap exists only for TE-like modes, and this can be seen in figure 2. In section 4.1.3 this characteristic of the photonic-crystal band structure will be revisited to explain an in-plane loss channel.

While frequency-domain simulations reveal highly accurate eigenfrequencies and modes, they cannot be used for time-dependent phenomena, such as  $Q$  calculations, and it is here that 3D FDTD simulations [10, 11] must be employed. Using these tools, we have modelled, fabricated and characterized

**Table 1.** Parameter summary of typical cavity designs obtained by 3D FDTD tools.  $r'$  refers to the radius of the perturbed holes.  $\lambda$ ,  $V$ ,  $n$  refer to the mode wavelength, mode volume and slab refractive index, respectively.

	$(\frac{d}{a}, \frac{r}{a}, \frac{s}{a}, \frac{r'}{a})$	$(\frac{a}{\lambda}, Q, \frac{V}{(\lambda n)^3})$
L0	(0.75, 0.30, 0.14, 0.30)	(0.287, 71 000, 0.122)
L1	(0.50, 0.35, 0.10, 0.25)	(0.300, 323 740, 0.422)
L3	(0.75, 0.30, 0.17, 0.30)	(0.247, 67 315, 0.392)

several cavity designs that feature high  $Q$ s and low  $V$ s; L3 [6], L1 [12] and L0 [13] cavity geometries (see figure 1(c)). Table 1 summarizes the various salient features of these cavities.

The regime of strong coupling [14] is entered when the coupling strength,  $g$ , between the QD and the cavity mode exceeds the average of the individual decay rates of the QD,  $\gamma$ , and the cavity mode,  $\kappa$ , i.e.  $2g > (\gamma + \kappa)/2$ . The motivation to choose a high  $Q$  comes from the fact that  $\kappa \propto 1/Q$ , while the need for a low  $V$  comes from the fact that  $g \propto 1/\sqrt{V}$ . To apply these cavity designs for cQED, special care must be taken to optimize both spatial and spectral overlap between a single QD and a cavity mode. Specifically, the placement of a QD at positions very close to the GaAs surfaces must be avoided, since coupling to surface states [15] will lead to strong non-radiative losses. In light of these considerations, the L3 mode which has the highest electric-field intensity at the cavity centre (see figure 1(c)) seems to be the most promising candidate for cQED experiments.

### 3. Fabrication and optical characterization

The GaAs material in which these resonators are fabricated is grown by molecular beam epitaxy (MBE). Details of this growth are provided elsewhere [16]. We typically start with a blank (001)-oriented GaAs wafer, onto which a 300 nm GaAs buffer is grown, followed by a 1  $\mu\text{m}$  thick sacrificial layer of the type  $\text{Al}_x\text{Ga}_{1-x}\text{As}$  (with  $0.7 \leq x \leq 0.94$ ), a 90 nm GaAs bottom slab, an atomic monolayer thick wetting layer on which form InAs QDs and finally a 90 nm GaAs top slab. It must be noted that, in the above-described scheme, dot growth is strain-induced and hence has a spatially probabilistic distribution. Further, minute variations in QD dimensions across the wafer give rise to a spectral distribution of emission wavelengths, typically a 5% spread about a 1  $\mu\text{m}$  central wavelength. It is worth mentioning here that the QD has an electric-field polarization that is primarily in-plane and thus couples to the TE-like (even) modes of the photonic crystal.

Fabrication of photonic-crystal cavities involves the following steps: cleaning of the top of the grown GaAs wafer surface, spinning and baking of an electron-beam resist, electron-beam lithography and subsequent resist development, pattern transfer into the substrate using a chemically assisted ion beam etch (CAIBE), removal of the underlying sacrificial layer by a suitable wet etch and a final strip of the remnant resist.

The first step in device fabrication is the removal of any organic material from the top GaAs surface using acetone and iso-propyl-alcohol (IPA). Any GaAs surface that has been

exposed to atmospheric oxygen forms a thin oxide layer and this is removed by immersing the wafer in a dilute solution of hydrochloric acid (HCl) (1:1 = HCl:deionized water (DI) by volume) for 10 min. After blow drying with  $\text{N}_2$  gas and heating on a hot plate at  $170^\circ\text{C}$  for at least 10 min, the wafer is ready for the spinning on of a thin layer of resist. Targeting a thickness of 150 nm, a high molecular-weight positive electron beam resist (950 K poly-methyl-methacrylate (PMMA) in anisole solvent) is spun on to the wafer and baked on a hot plate kept at  $170^\circ\text{C}$  for 30 min. Electron-beam lithography is then performed using a Vistech EBPG-5000+ 100 kV machine that is able to expose the device masks at a resolution of 2.5 nm. Employing a low beam current in the region of 800 pA accomplishes the proper exposure of the device masks. The exposed wafer is developed for 1 min in a solution of 1:3 = methyl-iso-butyl-ketone (MIBK):DI, followed by a 30 s rinse in IPA and a gentle  $\text{N}_2$  blow dry. The developed devices are inspected in an SEM to confirm proper exposure and adequate development.

The developed devices are then dry etched in a CAIBE for 3 min. The etcher uses a Kaufman ion source that ionizes a 4 standard-cubic-centimetres-per-minute (sccm) flow of argon gas at a beam voltage and current of 600 V and 25 mA, respectively.  $\text{Cl}_2$  gas is injected into the chamber just above the sample at a flow rate of 7 sccm. At the completion of the etch, the sample is immediately wet etched in a dilute solution of hydrofluoric acid (HF) (1:10 = HF:DI by volume) for 60 s, rinsed in DI and IPA for 60 s each and allowed to dry. The sample is then agitated in a solution of IPA, chloroform and acetone (1:1:1 by volume) for 10 min to strip the resist. This removes all of the resist, except for the regions around the devices. The sample is then exposed to a gentle oxygen plasma treatment for complete resist removal. An Oxford Instruments ICP-RIE 180 is used to perform this treatment for 90 s, employing an  $\text{O}_2$  flow rate of 90 sccm in a chamber at 10 mTorr, a low RF field (1 W) and a very high ICP power (600 W) that results in a gentle  $\text{O}_2$  plasma that keeps the DC bias below 20 V. This is important in minimizing any surface damage that can be caused by the procedure.

The fabricated devices are placed in an evacuated liquid helium cryostat, cooled down to approximately 10 K and excited by a non-resonant Ti:sapphire laser operating at 780 nm with an approximate power of 500  $\mu\text{W}$ . Photoluminescence from excited cavities is collected by a (36 $\times$ ) microscope objective, passed through a spectrometer and recorded on either an Si detector (for wavelengths  $<1 \mu\text{m}$ ) or an InGaAs detector (for wavelengths  $>1 \mu\text{m}$ ). Figure 3(a) shows the photoluminescence observed from a high  $Q$  cavity. A Lorentzian fit is used to calculate the  $Q$ .

Through careful  $Q$  measurements on a large set of fabricated devices, it is found that the measured  $Q$  values are not as high as computed, even though fabricated devices look nearly perfect in all aspects; side-wall roughness, circularity of holes, etc (see figure 3(b)). The following sections will be devoted to discussions of possible factors limiting  $Q$  based on practical considerations.

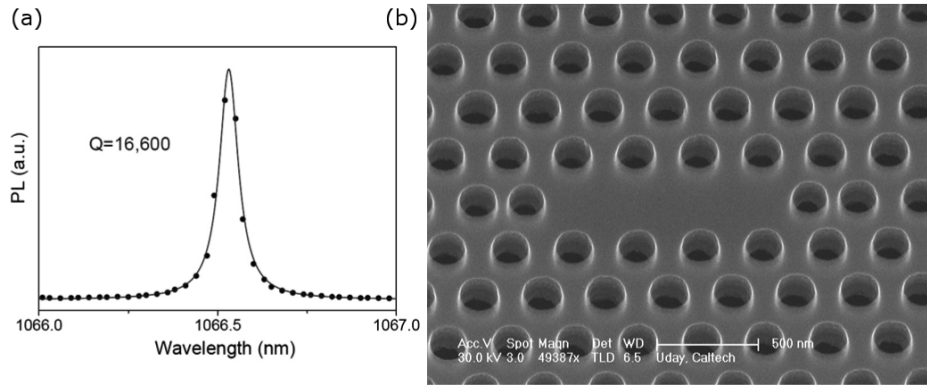


**Figure 3.** (a) Photoluminescence from a photonic-crystal cavity showing a Lorentzian fit to the data for the highest  $Q$  recorded. (b) Tilted SEM image of a fabricated L3 device.

#### 4. Quality factor considerations

As has been discussed elsewhere [17], the  $Q$  of a device can be decomposed into the following factors;

$$Q^{-1} = Q_{\text{rad}}^{-1} + Q_{\text{mat}}^{-1},$$

where  $Q_{\text{rad}}^{-1}$  indicates the optical loss from the cavity by coupling to radiation modes in vacuum and  $Q_{\text{mat}}^{-1}$  represents a combination of the intrinsic loss in the material, the loss due to the formation of surface states that inevitably result from the oxygen termination of broken dangling GaAs bonds at the etched interfaces and any gain or loss [18] that might occur due to QD absorption in the cavity's spectral and spatial neighbourhood. The loss represented by  $Q_{\text{mat}}^{-1}$  is strongly wavelength-dependent. On the one hand, GaAs shows increased loss [17] due to (sub-bandgap) surface states as one approaches the GaAs band edge at  $\approx 814$  nm (at 10 K). Simultaneously, at wavelengths close to and lower than the QD ensemble peak (typically between 950 and 1100 nm), absorption by the QDs and the wetting layer further degrades  $Q$  from the 'empty' (no QD) cavity  $Q$  [18].  $Q_{\text{rad}}^{-1}$  can be further divided into two terms,  $Q_0^{-1}$  and  $Q_{\text{scat}}^{-1}$ , where  $Q_0^{-1}$  indicates the intrinsic radiation loss in the absence of any fabrication-related error while  $Q_{\text{scat}}^{-1}$  is the loss due to (Rayleigh) scattering from surface imperfections introduced during MBE growth and device fabrication. To start with, fabrication-related failure modes that are fairly evident are presented, before moving on to  $Q$ -degrading factors that might not be obvious.

##### 4.1. Factors related to the fabrication failure modes

**4.1.1. Irregular shapes and positions of the air holes.**  $Q_0$  is optimized by a careful control of the cavity geometry and, in the case of L3 designs, can be theoretically as high as 67 000 in GaAs. (Higher  $Q$ s have been reported with photonic-crystal waveguide-type designs, but they are not considered here because of their higher mode volumes (calculated [19] as  $V \equiv [\int_V \epsilon(\vec{r}) |\vec{E}(\vec{r})|^2 d^3r] / \max[\epsilon(\vec{r}) |\vec{E}(\vec{r})|^2]$ ). Any irregularities in the lithography or etching can severely degrade  $Q_{\text{rad}}$ . A poorly focused electron beam can be a major cause of lithographic irregularities, with the photonic-crystal holes deviating from

circular shapes, as well as exposing areas larger than intended. Unless carefully controlled, the lithography step can also lead to considerable lack of reproducibility. Figure 4(b) illustrates the above-mentioned effects featuring non-circular and larger-than-intended holes which lead to the merging of holes that are closer than the lattice constant.

**4.1.2. Remnant PMMA and debris.** A thin layer of resist, as seen in figure 4(c) (darker, wrinkled features), is often left behind even after chemical treatment for removal. In our experience, this last layer of resist can only be removed by an oxygen plasma treatment. Moreover [16], a fine layer of submicron-sized microcrystallites is sometimes left behind after the completion of resist removal. These particles were speculated to be a hydroxide of aluminium that formed during the HF wet etch and floated from the sacrificial layer and ultimately were deposited on the top of the remnant resist. A 150 s dip in a solution of potassium hydroxide (KOH) (25 g/100 ml DI) was effective in completely removing this debris to restore the top surface to near-atomic smoothness. In terms of device performance,  $Q$ s were found to increase [16] on average by 50% after this KOH treatment, indicating that the debris was a very significant source of scattering loss. In subsequent fabrication runs, this KOH step was incorporated in the fabrication sequence right after the HF wet etch. Figure 4(a) shows a tilted view of a surface with debris prior to the KOH treatment and figure 3(b) shows a fully fabricated device. Finally, roughness and ion-induced side-wall damage are introduced to the surfaces during the CAIBE etch which can further contribute to scattering. It is not possible to quantify the contribution of the latter source of scattering at this point, as the surfaces seem fairly smooth even in high resolution SEMs.

**4.1.3. Non-vertical side-walls.** Maintaining a vertical etch profile in the dry etch is also important [20]. As explained in section 2, the presence of mirror symmetry in the case of perfectly vertical side-walls allows one to classify slab modes into even and odd symmetry modes. However, non-verticality of etched air holes breaks this symmetry, which results in new forms of hybridized modes that can no longer be classified as

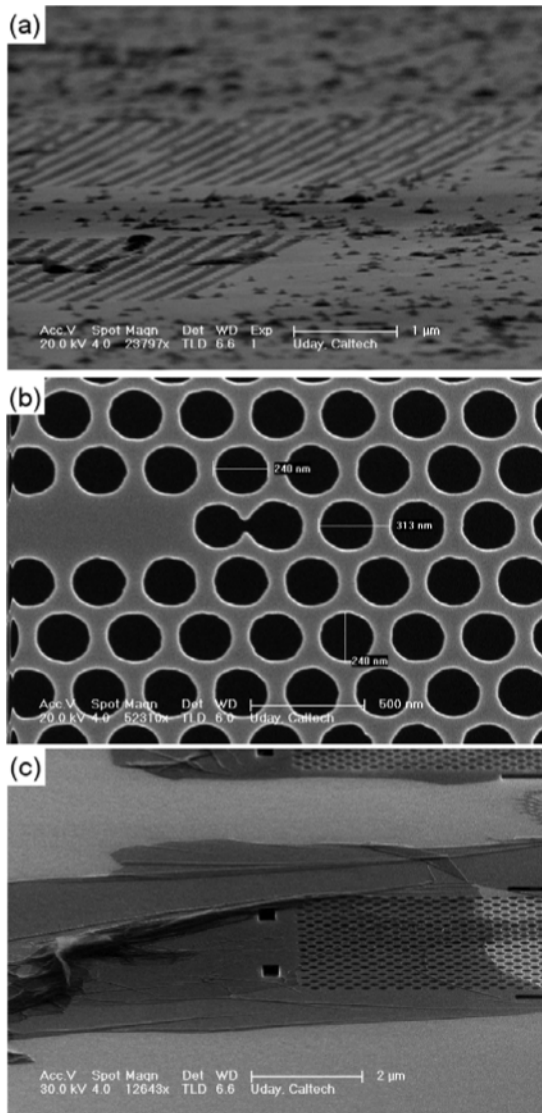


**Figure 4.** (a) SEM of a tilted slab showing the presence of fine debris after undercutting with HF. (b) SEM showing the effects of poor lithography on a photonic-crystal cavity. (c) SEM of a tilted L3 cavity showing remnant resist (dark, wrinkled features).

either even or odd. A deviation from a vertical etch by even  $2^\circ$  can cause  $Q_{\text{rad}}$  to drop by an order of magnitude and this is due to the well-known TE–TM coupling loss [21]. There are at least two factors that can cause non-vertical side-walls. Firstly, inadequate or excessive resist development can give rise to non-vertical resist side-walls, which in turn are transferred to non-vertical side-walls in the GaAs substrate. Secondly, a non-vertical flow of  $\text{Cl}_2$  gas onto the substrate during the dry etch in the CAIBE can lead to asymmetric and non-vertical side-walls. Small-angle deviations ( $\leq 2^\circ$ ) from the vertical are hard to measure with the available resolution in an SEM, making it difficult to precisely quantify this loss channel. In general, it is easier to control etch symmetry and verticality using a plasma etch, such as in an inductively coupled plasma-reactive ion etcher (ICP-RIE). Additionally, the use of photonic crystals with a complete photonic bandgap for both TE-like and TM-like modes can reduce the severity of a non-vertical

etch. Significant results have been achieved using reduced symmetry photonic crystals [22–24], although in general, the spectral extent of the TM-like bandgap is much less than that of the TE-like counterpart.

#### 4.2. Effect of a bottom substrate

Removal of the AlGaAs sacrificial layer below the photonic-crystal slab creates an air gap, exposing an optically flat surface. It is important for this air gap to be at least greater than half the vacuum wavelength to reduce optical loss into the substrate. It should be noted that reflectivity at the GaAs substrate is  $\sim 30\%$ . Therefore, the effect of a bottom substrate is essentially that of a reflector below the photonic-crystal mode. For an air-gap size larger than half the vacuum wavelength, there can be multiple non-negligible reflections between the photonic-crystal slab and substrate. Thus, a fraction of the originally downward-emitted photons from the cavity are redirected upward by the bottom reflector to interfere with the originally upward-emitted photons. As a result, the far-field radiation pattern of the cavity mode is modified, changing the total emitted power [25, 26]. This is analogous to the well-known cQED example of a point dipole source in front of a mirror [27]. By changing the distance between the dipole source and the mirror, the original decay rate and radiation pattern are modified. Analogously, the  $Q$  of the cavity mode changes as a function of the air-gap size.

In figure 5 the  $Q$  of the L3 cavity mode is calculated by varying the air-gap size,  $t$ . Even when  $t \geq 800$  nm,  $Q$  varies by about  $\pm 5\%$  around  $Q_\infty$  (where  $Q_\infty = 67315$  obtained in the absence of a bottom substrate). A larger variation in  $Q$  can be obtained by starting with a cavity mode that has a smaller  $Q_\infty$ , since more radiative power will contribute to far-field interference. Through additional FDTD simulations, it is found that a  $Q$  variation larger than  $\pm 10\%$  is expected when  $Q_\infty \sim 50000$ . Therefore, the AlGaAs sacrificial layer thickness should be chosen carefully if  $Q$  is of primary concern in the design of photonic-crystal cavities.

#### 4.3. Contour FDTD simulation

Although the theoretical cavity  $Q$ s can be as high as 67 000, less than half this number has been experimentally observed (see figure 3(a)). To investigate this discrepancy, the use of a 2D contour image extracted from the SEM image of a fabricated device for the purposes of  $Q$  estimation is proposed.

Let us consider the particular case of a fabricated L3 cavity whose resonant wavelength and  $Q$  are measured to be 1144.1 nm and 10 050, respectively. First, all the structural parameters ( $r$ ,  $r'$ ,  $s$  and  $a$ ) characterizing the cavity are extracted from the corresponding SEM image (It should be noted that there can be  $\sim \pm 5\%$  error in the SEM scale.). 3D FDTD simulations based on these parameters reveal a resonant wavelength and  $Q$  of 1129.7 nm and 31 418, respectively. Clearly,  $Q$  values estimated in this way differ significantly from the measured  $Q$ .

Instead, contour data that faithfully captures all the fabrication-related imperfections (instead of using averaged cavity parameters from the SEM image) can be employed in

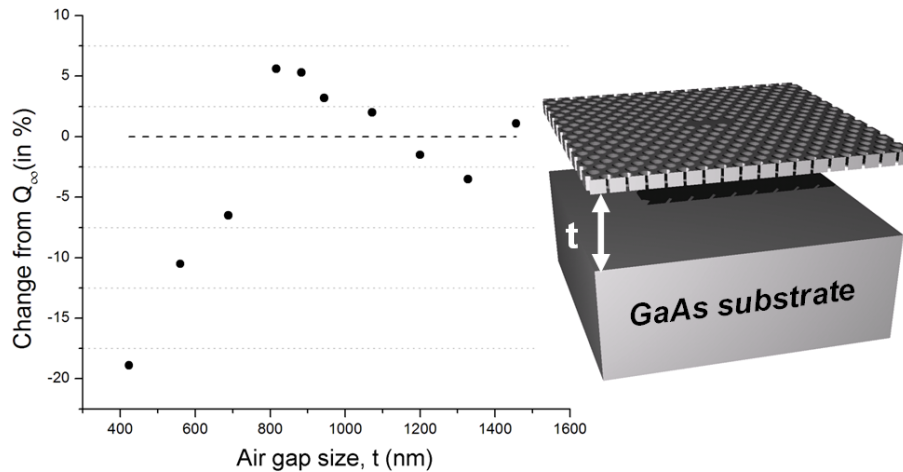


**Figure 5.** Variation of  $Q_{\text{rad}}$  with slab-to-substrate air gap for a slab of thickness 190 nm and a cavity mode at 1026 nm. (The other device parameters are the same as the L3 cavity shown in table 1.) The dashed line corresponds to  $Q_\infty = 67\,315$  when there is no substrate in the vicinity of the slab. All data is obtained by 3D FDTD tools

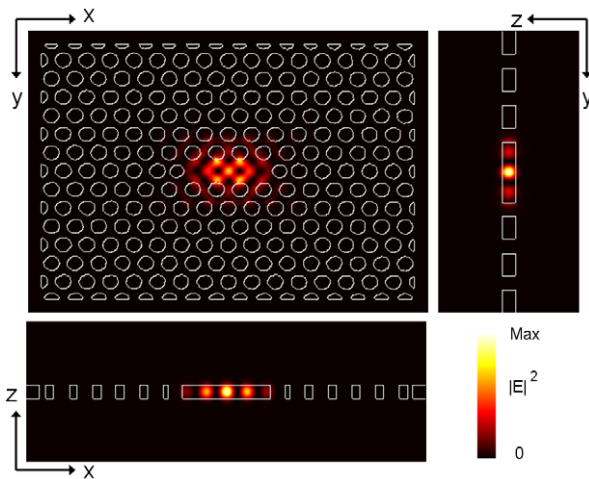


**Figure 6.** Electric-field intensity profiles from a contour FDTD simulation (contour data superimposed) for the three symmetry planes of the photonic-crystal cavity.

3D FDTD simulations [28]. As is evident from figure 1(c), the electric-field intensity distribution ( $|\vec{E}(\vec{r})|^2$ ) of the L3 mode reveals strongly localized patterns around the four air holes nearest to the cavity centre. Recalling the fact that the  $Q$  of the L3 mode is highly sensitive to the fine tuning of the nearest air holes [6], even minute deviations from the ideal geometry can severely degrade  $Q_{\text{scat}}$  and this can be quantified using contour FDTD.

The extracted contour plot and simulated  $|\vec{E}(\vec{r})|^2$  for the structure mentioned above are shown in figure 6, in which a grid resolution of  $\Delta x = \Delta y = \Delta z \approx 10$  nm is employed [10]. The  $Q$  obtained in this way drops to 21 283, which is still large but becomes closer to the measured value of 10 050. The remaining discrepancy can be attributed to non-vertical air holes, side-wall roughness and material losses that cannot be incorporated in a contour FDTD simulation. Finally, for a more realistic  $Q$  value, an air gap and GaAs substrate are included. The  $Q$  value in the presence of a 800 nm air gap is

23 576, showing about 10% improvement in comparison with the structure without the air gap.

#### 4.4. Crystal-axis-dependent surface roughness

As we have recently reported [16], the underside of the GaAs slab can have wavy undulations that show an RMS roughness of the order of 25 nm, while maintaining an extremely smooth top surface. First by transmission electron microscopy, and then by atomic force microscopy (AFM), it was observed that the magnitude of the roughness was greater along the [110] direction than the  $[\bar{1}\bar{1}0]$  direction. To test whether this crystal-axis-dependent roughness had any bearing on cavity  $Q$ s, several pairs of identical cavities were fabricated with the cavity long axis (the line joining the  $s$ -shifted holes in the case of the L3 designs) aligned along either of the directions mentioned above. It was found that, on average, cavities whose axis was aligned along the lower roughness direction had  $Q$ s that were 20–32% less (see figure 7(b)) than those aligned along the higher roughness direction. It must be noted that the overall  $Q$ s recorded in this experiment were low, on account of angled (non-vertical) walls of the photonic-crystal holes. Figure 7(a) shows the AFM scan of one such low  $Q$  cavity. Growth improvements [16] have been detailed to ensure top and bottom slab surfaces with atomic smoothness and minimal contribution to scattering loss.

## 5. Conclusion

Several factors contributing to photon loss from photonic-crystal cavities designed for cQED experiments are identified and addressed. Among them are irregularities with fabrication, crystal-axis-dependent losses and the presence of a bottom substrate. Lithography issues can be corrected by ensuring a properly focused electron beam; etched side-walls can be made vertical by careful control of the  $\text{Cl}_2$  flow direction during dry etch; crystal-axis-dependent losses can be eliminated by optimized growth that leads to smooth slab interfaces; remnant

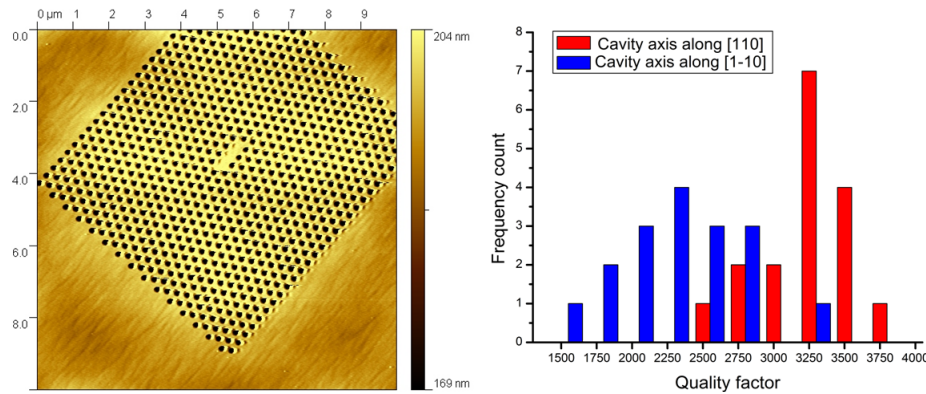


**Figure 7.** (a) Atomic force micrograph of a low  $Q$  L3 cavity whose axis is aligned along the low roughness crystal axis  $[1\bar{1}0]$  (running from bottom left to top right in the image). (b) Histogram for  $Q$  values corresponding to the two different orientations of cavity and crystal axis.

resist can be removed by an oxygen plasma; debris left behind by the HF undercut can be removed by treating with KOH. Careful choice of sacrificial (AlGaAs) layer thickness can enhance cavity  $Q$ . The use of contour FDTD as a diagnostic tool for estimating cavity  $Q$ s is highlighted.

### Acknowledgments

The authors gratefully acknowledge support (EEC-0812072) from the National Science Foundation (NSF) through the Engineering Research Center for Integrated Access Networks (CIAN). The Caltech authors acknowledge critical support and infrastructure provided for this work by the Kavli Nanoscience Institute at Caltech. The Tucson group also acknowledges support from NSF Atomic Molecular and Optical Physics (AMOP) and Electronics, Photonics and Device Technologies (EPDT), AFOSR, and Arizona Technology and Research Initiative Funding (TRIF). HMG thanks the Alexander von Humboldt Foundation for a Renewed Research Stay.

### References

- [1] Yablonovitch E 1987 *Phys. Rev. Lett.* **58** 2059–62
- [2] John S 1987 *Phys. Rev. Lett.* **58** 2486–9
- [3] Englund D, Fattal D, Waks E, Solomon G, Zhang B, Nakaoka T, Arakawa Y, Yamamoto Y and Vuckovic J 2005 *Phys. Rev. Lett.* **95** 013904
- [4] Yoshie T, Scherer A, Hendrickson J, Khitrova G, Gibbs H M, Rupper G, Ell C, Shchekin O B and Deppe D G 2004 *Nature* **432** 200–3
- [5] Press D, Gotzinger S, Reitzenstein S, Hofmann C, Löffler A, Kamp M, Forchel A and Yamamoto Y 2007 *Phys. Rev. Lett.* **98** 117402
- [6] Akahane Y, Asano T, Song B-S and Noda S 2003 *Nature* **425** 944–7
- [7] Painter O, Vuckovic J and Scherer A 1999 *J. Opt. Soc. Am. B* **16** 275–85
- [8] Johnson S G and Joannopoulos J D 2001 *Opt. Express* **8** 173–90
- [9] Johnson S G, Fan S, Villeneuve P R, Joannopoulos J D and Kolodziejski L A 1999 *Phys. Rev. B* **60** 5751
- [10] Farjadpour A, Roundy D, Rodriguez A, Ibanescu M, Bermel P, Joannopoulos J D, Johnson S G and Burr G 2006 *Opt. Lett.* **31** 2972–4
- [11] Mandelshtam V A and Taylor H S 1997 *J. Chem. Phys.* **107** 6756–69
- [12] Park H G, Hwang J K, Huh J, Ryu H Y, Kim S-H, Kim J S and Lee Y-H 2002 *IEEE J. Quantum Electron.* **38** 1353
- [13] Nozaki K and Baba T 2006 *Appl. Phys. Lett.* **88** 211101
- [14] Khitrova G, Gibbs H M, Kira M, Koch S W and Scherer A 2006 *Nat. Phys.* **2** 81–90
- [15] Strauf S, Hennessy K, Rakher M T, Choi Y S, Badolato A, Andreani L C, Hu E L, Petroff P M and Bouwmeester D 2006 *Phys. Rev. Lett.* **96** 127404
- [16] Sweet J *et al* 2009 *Photon. Nanostruct. Fundament. Appl.* doi:10.1016/j.photonics.2009.10.004
- [17] Michael C P, Srinivasan K, Johnson T J, Painter O, Lee K H, Hennessy K, Kim H and Hu E 2007 *Appl. Phys. Lett.* **90** 051108
- [18] Hendrickson J *et al* 2005 *Phys. Rev. B* **72** 193303
- [19] Villeneuve P R, Fan S, Johnson S G and Joannopoulos J D 1998 *IEE Proc. Optoelectron.* **145** 384
- [20] Kim M-K, Yang J-K, Lee Y-H and Hwang I-K 2007 *J. Korean Phys. Soc.* **50** 1027–31
- [21] Tanaka Y, Asano T, Akahane Y, Song B-S and Noda S 2003 *Appl. Phys. Lett.* **82** 1661–3
- [22] Takayama S-T, Kitagawa H, Tanaka Y, Asano T and Noda S 2005 *Appl. Phys. Lett.* **87** 061107
- [23] Wen F, David S, Checoury X, Kurdi M E and Boucaud P 2008 *Opt. Express* **16** 12278–89
- [24] Ohlinger K, Lun Y and Qualls J S 2009 *J. Appl. Phys.* **106** 063520
- [25] Kim S-H, Kim S-K and Lee Y-H 2006 *Phys. Rev. B* **73** 235117
- [26] Vuckovic J, Englund D, Fattal D, Waks E and Yamamoto Y 2006 *Physica E* **32** 466–70
- [27] Hinds E A 1994 *Cavity Quantum Electrodynamics* ed P R Berman (New York: Academic)
- [28] Englund D and Vuckovic J 2006 *Opt. Express* **14** 3472–83